A multilayer control for multirotor UAVs equipped with a servo robot arm

F. Ruggiero[1], M.A. Trujillo[2], R. Cano[2], H. Ascorbe[2], A. Viguria[2], C. Peréz[2], V. Lippiello[1], A. Ollero[3], and B. Siciliano[1]

***Abstract*— A multilayer architecture to control multirotor UAVs equipped with a servo robot arm is proposed in this paper. The main purpose is to control the aerial platform taking into account the presence of the moving manipulator. Three layers are considered in this work. First, a novel mechanism is proposed considering a moving battery to counterweight the statics of the robotic arm. Then, in order to overcome the mechanical limitations of the previous layer, the residual of the arm static effects on the UAV is computed and compensated through the given control thrust and torques. Finally, an estimator of external forces and moments acting on the aerial vehicle is considered and the estimations are fed back to the controller to compensate neglected aerodynamic effects and the arm dynamics. The performance of the proposed architecture has been experimentally evaluated.**

I. INTRODUCTION

Aerial manipulation is a growing field inside robotic research. Unmanned aerial vehicles (UAVs) are increasingly employed in active tasks such as grasping and manipulation. For this reason, the presence of *aerial manipulators* –a multirotor UAV equipped with a n-DoF (degrees of freedom) robotic arm– is augmenting inside robotic labs. An aerial manipulator merges the versatility of multirotor UAVs with the precision of robotic arms. However, the coupling effects between the aerial vehicle and the manipulator arise several modelling and control problems.

In general, two approaches can be thought to control an aerial manipulator. The former considers the multirotor and the robotic arm as a unique entity, and thus the controller is designed on the basis of the complete dynamic model [1], [2]. The latter considers the UAV and the arm as two separate and independent systems. The effects of the arm on the multirotor are seen as external disturbances and viceversa. This approach might be useful in case the reactivity of the arm is not enough to compensate the UAV position errors and/or in case the arm does not allow torque control.

The research leading to these results has been supported by the ARCAS collaborative project, which has received funding from the European Community Seventh Framework Programme (FP7/2007-2013) under grant agreement ICT-287617. The authors are solely responsible for its content. It does not represent the opinion of the European Community and the Community is not responsible for any use that might be made of the information contained therein.

[1]PRISMA Lab, Department of Electrical Engineering and Information Technology, University of Naples, Via Claudio 21, 80125, Naples, Italy.

[2]Center for Advanced Aerospace Technologies (CATEC), C/ Wilbur y Orville Wright 19, 41309, La Rinconada, Sevilla, Spain.

[3]Systems Engineering and Automatic Control Department, University of Seville, Camino de los Descubrimientos s/n, 41092, Seville, Spain.

Contact emails fabio.ruggiero@unina.it, matrujillo@catec.aero

Focusing on the latter approach, the control of the UAV and the one of the robotic arm are thus, at least partially, treated separately. On one hand, the control of the sole aerial platform has been extensively addressed during last years: backstepping [3], [4], optical flow [5], vision [6], port-Hamiltonian [7], etc. On the other hand, the control of robotic manipulators is well settled in the literature [8].

Inside the ARCAS project [9], that proposes the development of a cooperative free-flying robot systems for assembly and structure construction, the control of an aerial vehicle equipped of a robotic arm is crucial. The identified solution within ARCAS has been to employ a modular architecture for the robotic arm using off-the-shelf servomotors.

In this paper, a multilayer control system is proposed aiming at reducing the effects of the movements of the robotic arm at the CoG (center of gravity) of the multirotor. The addition of each layer is analysed and the related benefits are compared. Namely, three layers are considered: first, a novel mechanism is introduced whose purpose is to move the multirotor's battery to counterweight the arm movements; second, in order to overcome mechanical limits of the previous mechanism, the residual static momentum induced by the manipulator's gravity on the multirotor is compensated by the propellers; third, an estimator of external generalized forces (forces plus moments) acting on the multirotor is implemented, and the resulting estimation is fed back to the controller to compensate everything else has not been taken into account in the previous layers, e.g., arm dynamics, wind, turbulence of the air flow caused by the presence of the arm, external forces due to the interaction of the arm with the environment, and so on. The basic layer, that is always active, is a classic PID controller for the multirotor.

Despite the paper is focused on the architecture developed within the ARCAS project, the subject of this work remains general since it might be applied to any kind of aerial manipulator equipped with servomotors. The main contributions of the paper are then highlighted in the following list. 1) The proposed multilayer control is one among the first practical approaches analysing the effects of a moving robotic arm mounted on an aerial platform, considering these two systems as separate entities. Other approaches [1], [2], [10], [11], [12] rely instead on the complete dynamic model of the aerial manipulator allowing directly control of the manipulator joint torques. 2) The moving battery compartment is a novelty in this field. Several solutions to change the CoG position have been found for aerial systems, some even used in commercial applications. The best known

is the fuel transfer between different tanks in aircrafts, for example, in some Airbus models such as the A380 or A340. Patent [13] describes a system that redistributes the load when a part of it is released, modifying the CoG of the UAV. Nevertheless, this system is applicable only to slung load and not for load manipulation. It has not found in the previous bibliography any invention for compensating the CoG displacement during load manipulation with a robotic arm on board a UAV. 3) Estimators of external generalized forces acting on a UAV have been introduced in [14], [15]. Differently from [14], in this paper the measure of the angular velocity is directly employed to make the estimator less dependent from the representation of the rotations.

The outline of the paper is as follows. Next section introduces the general modelling of an UAV. The proposed multilayer control system is introduced in Section III. Section IV presents an experimental validation of the proposed approach, focusing on the ARCAS equipment in Section IV-A, and its general architecture in Section IV-B. Finally, Section V concludes the paper.

II. Modelling

Define a world-fixed inertial frame $\{O, X, Y, Z\}$ and a body-fixed frame $\{O_b, X_b, Y_b, Z_b\}$ placed at the multirotor CoG. The absolute position of the multirotor with respect to the inertial frame is denoted by $\boldsymbol{p}_b \in \mathbb{R}^3$. Using the roll-pitch-yaw $(\phi,\ \theta,\ \psi)$ Euler angles, $\boldsymbol{\eta}_b \in \mathbb{R}^3$, the attitude of the body frame with respect to the inertial frame is represented through the rotation matrix $\boldsymbol{R}_b(\boldsymbol{\eta}_b) \in SO(3)$. The general dynamic model of a multirotor is given by [14]

$$\begin{cases} m\ddot{\boldsymbol{p}}_b + m\boldsymbol{g}_b = \boldsymbol{R}_b(\boldsymbol{\eta}_b)\left(\boldsymbol{f}_b^b + \boldsymbol{f}_v^b\right), & \text{(1a)} \\ \boldsymbol{I}_b\dot{\boldsymbol{\omega}}_b^b + \boldsymbol{S}(\boldsymbol{\omega}_b^b)\boldsymbol{I}_b\boldsymbol{\omega}_b^b = \boldsymbol{\tau}_b^b + \boldsymbol{\tau}_v^b, & \text{(1b)} \end{cases}$$

where $\ddot{\boldsymbol{p}}_b \in \mathbb{R}^3$ is the linear acceleration of the multirotor expressed in the inertial frame; m is the mass and $\boldsymbol{I}_b \in \mathbb{R}^{3\times3}$ is its constant diagonal inertia matrix expressed with respect to the body frame; $\boldsymbol{\omega}_b^b \in \mathbb{R}^3$ and $\dot{\boldsymbol{\omega}}_b{}^b \in \mathbb{R}^3$ are the angular velocity and acceleration, respectively, of the multirotor expressed in the body frame; $\boldsymbol{S}(\cdot) \in \mathbb{R}^{3\times3}$ denotes the skew-symmetric matrix; $\boldsymbol{g}_b = \begin{bmatrix}0 & 0 & 9.81\end{bmatrix}^{\mathrm{T}}$ is the gravity vector; $\boldsymbol{f}_b^b \in \mathbb{R}^3$ and $\boldsymbol{\tau}_b^b \in \mathbb{R}^3$ are the forces and torques input vectors, respectively; $\boldsymbol{f}_v^b \in \mathbb{R}^3$ and $\boldsymbol{\tau}_v^b \in \mathbb{R}^3$ represent external forces and torques, respectively, acting on the aerial vehicle and expressed in the body frame. Such external disturbances are generally produced by: effects of the arm's movements on the multirotor; neglected aerodynamic effects; physical interaction of the system with the environment. Depending on the particular configuration of the available multirotor, the expressions of $\boldsymbol{f}_b^b$ and $\boldsymbol{\tau}_b^b$ are different. In the quadrotor case, it is possible to consider $\boldsymbol{\tau}_b^b = \begin{bmatrix}\tau_\phi & \tau_\theta & \tau_\psi\end{bmatrix}^{\mathrm{T}}$ and $\boldsymbol{f}_b^b = \begin{bmatrix}0 & 0 & u\end{bmatrix}^{\mathrm{T}}$, where u denotes the total thrust perpendicular to the propellers plane. The relationship between the thrust and the control torques with the force generated by each propeller depends on many aerodynamic effects (drag effects, distance of the propellers from the multirotor CoG, number of the rotors, etc.) [16].

III. Multilayer Control System

The problem of controlling a multirotor with an equipped moving arm is addressed in this section by employing a multilayer control system. Roughly speaking, the resulting control law for the multirotor (1) is given by the contribution of the layers described in the Introduction

$$u = f_u(\boldsymbol{g}_b, \boldsymbol{f}_0, \boldsymbol{f}_2, \boldsymbol{f}_3), \quad \text{(2a)}$$

$$\boldsymbol{\tau}_b^b = \boldsymbol{f}_\tau(\boldsymbol{\tau}_0, \boldsymbol{\tau}_2, \boldsymbol{\tau}_3), \quad \text{(2b)}$$

where $\boldsymbol{f}_0 \in \mathbb{R}^3$ and $\boldsymbol{\tau}_0 \in \mathbb{R}^3$ are the basic PID control actions for the quadrotor position and attitude, respectively, and described in Section IV-B (layer 0); $\boldsymbol{f}_i \in \mathbb{R}^3$ and $\boldsymbol{\tau}_i \in \mathbb{R}^3$ are the force and torque control actions due to the ith layer, with $i = 2, 3$[1]; $f_u(\cdot) \in \mathbb{R}$ and $\boldsymbol{f}_\tau(\cdot) \in \mathbb{R}^3$ are two, generally nonlinear, functions to calculate the thrust and the multirotor control torques, respectively. On one hand, the particular expression for f_u might depend on the chosen parametrization of rotation, i.e., Euler angles, unit quaternion, and so on (see [16]). On the other hand, the expression for $\boldsymbol{f}_\tau$ can be generally considered as a (weighted) sum of each contribution $\boldsymbol{f}_\tau = \beta_0\boldsymbol{\tau}_0 + \beta_2\boldsymbol{\tau}_2 + \beta_3\boldsymbol{\tau}_3$, with β_i, $i = \{0, 2, 3\}$, the associated weights. The detail description of all the control layers follows in the sequent subsections.

A. Battery Movement Compensation

Generally, a manipulator consists of three components, namely a fixed base, a multi-joint arm and an end effector (see Fig. 1). In this case, the base is an auxiliary component fixed to the landing gear that supports the arm and also hosts the CoG Displacement Compensation System (DCS). This DCS consists of a counterweight that is moved on a linear slider during the manipulator operation to keep the CoG of the whole system (UAV + manipulator + load + counterweight) as close as possible to the multirotor geometric center. This center is coincident with the CoG of the whole system when the robotic arm is retracted in its compact configuration. The on-board batteries are used as counterweights: they are heavy enough to compensate the manipulator CoG displacements with short movements.

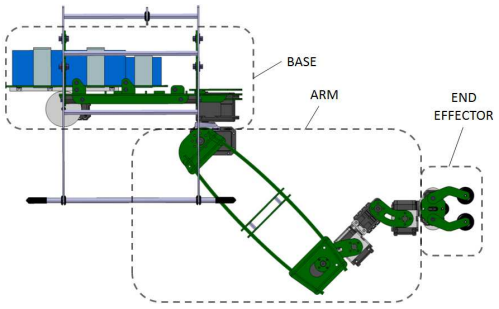

Fig. 1. Manipulator components (base, arm and end effector) mounted on multirotor landing gear.

[1]The effect of the first layer is instead given by a proper mechanism mounted on the aerial platform, i.e., the battery movement compensator.

The instantaneous CoG position of each link i, referred to the arm fixed axis system $\{O_0, X_0, Y_0, Z_0\}$, is given by

$$\begin{bmatrix} x^0_{Ai} & y^0_{Ai} & z^0_{Ai} & 1 \end{bmatrix}^{\mathrm{T}} = \boldsymbol{T}^0_i \begin{bmatrix} x^i_{Ai} & y^i_{Ai} & z^i_{Ai} & 1 \end{bmatrix}^{\mathrm{T}}, \quad (3)$$

for $i = 1, \ldots, 7$, where $\boldsymbol{T}^0_i \in \mathbb{R}^{4\times4}$ is the homogeneous transformation matrix of link i updated by the servos feedback. Notice that $i = 7$ corresponds to the payload grasped by the robotic arm.

The robotic arm CoG position vector $\boldsymbol{p}^b_A \in \mathbb{R}^3$ referred to the body frame is given by

$$\boldsymbol{p}^b_A = \frac{1}{m_A} \boldsymbol{E}_3 \boldsymbol{T}^b_0 \left(\sum_{i=1}^{7} m_i \begin{bmatrix} x^0_{Ai} & y^0_{Ai} & z^0_{Ai} & 1 \end{bmatrix}^{\mathrm{T}} \right), \quad (4)$$

where m_i is the ith link mass, $m_A = \sum_{i=1}^{7} m_i$, $\boldsymbol{T}^b_0 \in \mathbb{R}^{4\times4}$ is the constant homogeneous transformation matrix from arm to body frame and $\boldsymbol{E}_3 \in \mathbb{R}^{3\times4}$ selects the first three components. It is supposed that the CoG of the platform is coincident with its geometric center, so the position reference for the battery $\boldsymbol{p}^{b^*}_B \in \mathbb{R}^3$ is calculated with

$$m_A \boldsymbol{p}^b_A + m_B \boldsymbol{p}^b_B = \boldsymbol{0}_3 \rightarrow \boldsymbol{p}^{b^*}_B = (m_A/m_B) \boldsymbol{p}^b_A, \quad (5)$$

where $\boldsymbol{0}_3 \in \mathbb{R}^3$ is the zero vector, $\boldsymbol{p}^b_B \in \mathbb{R}^3$ is the CoG position of the battery in the body frame, and m_B is the battery mass. As the battery movement is linear, it can only achieve part of the gravity compensation. The reference given to the servo is the projection of $\boldsymbol{p}^{b^*}_B$ along the battery axis.

This system is really effective for slow motions of the robotic arm as it maintains the CoG of the full system very close to the geometric center. However it has two limitations: the former is the mechanical limits of the DCS; the latter is that the velocity of the compensation is not enough for not-too-fast operations because of servo limitations[2]

B. Arm Static Compensation

The above mentioned DCS limitations do not address the complete stabilization of the aerial manipulator. The battery can in fact reach a mechanical limit depending on the grasped load and the arm configuration, making impossible to fully counterweight the CoG displacement. Moreover, the battery reaches the desired position with a delay depending on how far it is from its actual position. Software compensation is then needed to properly modify the propellers velocity. The first approach is to perform static momentum equilibrium above the geometric center of the platform (see Fig. 2).

As it is considered that the platform performs hovering type flying while moving the robotic arm for manipulation tasks, any static torque around the yaw axis can be neglected

$$\boldsymbol{f}_2 = \boldsymbol{0_3}, \quad (6a)$$

$$\boldsymbol{\tau}_2 = \boldsymbol{E}_2 \left(m_A \boldsymbol{p}^b_A + m_B \boldsymbol{p}^b_B \right), \quad (6b)$$

where $\boldsymbol{E}_2 \in \mathbb{R}^{3\times3}$ selects the first two components putting the third to zero.

[2]With the available equipment, since the battery servo is limited to π rad/s, it has been experimentally estimated that the arm CoG component parallel to the slider can not be compensated if it moves faster than 15 cm/s.

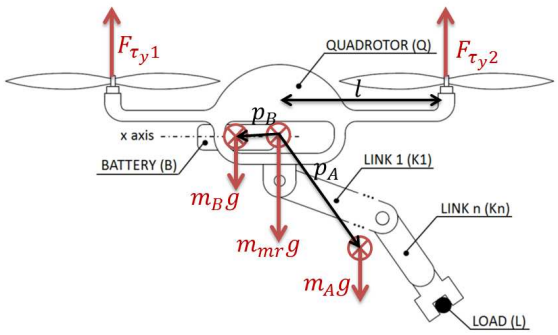

Fig. 2. Momentum equilibrium above the geometric center

The last part of this layer consists in the low level roll-pitch-yaw controller, an angular rates controller and a saturation of forces and torques. The Static Compensation (*SC*) module calculates the torques using (6) and they are injected directly after the angular rates controller which outputs are forces and torques.

This control scheme has proved to be very effective combined with the DCS system. However it leaves room for improvement as the robotic arm could be moved aggressively in order to manipulate effectively a load while different external perturbations (e.g., wind) excites the flying robot.

C. External Generalized Forces Estimation & Compensation

All the remaining not yet compensated dynamic effects of the manipulator on the aerial platform, plus the neglected aerodynamic terms, can be estimated through an estimator of external generalized forces and then fed back to the controller. The here proposed estimator has been modified with respect to [14] to be less dependent from the angular representation of rotations.

Following [14], [17], the generalized momentum vector $\boldsymbol{\alpha} \in \mathbb{R}^6$ of the system (1) is defined as

$$\boldsymbol{\alpha} = \begin{bmatrix} m\boldsymbol{I}_3 & \boldsymbol{O}_3 \\ \boldsymbol{O}_3 & \boldsymbol{I}_b \end{bmatrix} \begin{bmatrix} \dot{\boldsymbol{p}}_b \\ \boldsymbol{\omega}^b_b \end{bmatrix}, \quad (7)$$

where $\dot{\boldsymbol{p}}_b \in \mathbb{R}^3$ is the linear velocity of the multirotor in the inertial frame; $\boldsymbol{I}_m \in \mathbb{R}^{m\times m}$ is the identity matrix and $\boldsymbol{O}_m \in \mathbb{R}^{m\times m}$ is the zero matrix. Therefore, defining $\boldsymbol{e}_3 = \begin{bmatrix} 0 & 0 & 1 \end{bmatrix}^{\mathrm{T}}$, the time derivative of (7) is

$$\dot{\boldsymbol{\alpha}} = \begin{bmatrix} \boldsymbol{R}_b(\boldsymbol{\eta}_b) \left(u\boldsymbol{e}_3 + \boldsymbol{f}^b_v \right) - m\boldsymbol{g}_b \\ \boldsymbol{\tau}^b_b + \boldsymbol{\tau}^b_v - \boldsymbol{S}(\boldsymbol{\omega}^b_b)\boldsymbol{I}_b\boldsymbol{\omega}^b_b \end{bmatrix}. \quad (8)$$

Denoting with $\boldsymbol{r} = \begin{bmatrix} \boldsymbol{f}^{\mathrm{T}}_v & \boldsymbol{\tau}^{b^{\mathrm{T}}}_v \end{bmatrix}^{\mathrm{T}} \in \mathbb{R}^6$ the estimated generalized forces, the estimator can be built similarly to [14] as follows (see [14] for further details)

$$\boldsymbol{r}(t) = \boldsymbol{K}_1 \left(\int_0^t -\boldsymbol{r}(s) + \boldsymbol{K}_2 \left(\boldsymbol{\alpha}(s) - \int_0^t \left(\begin{bmatrix} u\boldsymbol{R}_b(\boldsymbol{\eta}_b)\boldsymbol{e}_3 - m\boldsymbol{g}_b \\ \boldsymbol{\tau}^b_b - \boldsymbol{S}(\boldsymbol{\omega}^b_b)\boldsymbol{I}_b\boldsymbol{\omega}^b_b \end{bmatrix} + \boldsymbol{r}(s) \right) ds \right) ds \right), \quad (9)$$

where t denotes the current time instant of estimation, $\boldsymbol{K}_1 \in \mathbb{R}^{6\times6}$ and $\boldsymbol{K}_2 \in \mathbb{R}^{6\times6}$ are two positive definite diagonal gain matrices, and it is assumed that $\boldsymbol{\alpha}(0) = \boldsymbol{r}(0) = \dot{\boldsymbol{r}}(0) = 0$.

The needed quantities to estimate the external generalized forces are the multirotor attitude $\boldsymbol{R}(\cdot)$ and angular velocity $\boldsymbol{\omega}_b^b$ given by the onboard IMU; the commanded thrust u and $\boldsymbol{\tau}_b^b$; the linear velocity $\dot{\boldsymbol{p}}_b$ estimated through vision and/or GPS data in outdoor scenarios, and through tracking systems in indoor cases; the multirotor mass m and inertia $\boldsymbol{I}_b$.

Hence, the final contribution of the layer is the feedback to the controller of the estimated external forces and moments

$$\boldsymbol{f}_3 = -\overline{\boldsymbol{E}}_3 \boldsymbol{r}, \tag{10a}$$

$$\boldsymbol{\tau}_3 = -\underline{\boldsymbol{E}}_3 \boldsymbol{r}, \tag{10b}$$

where $\overline{\boldsymbol{E}}_3 \in \mathbb{R}^{3\times 6}$ and $\underline{\boldsymbol{E}}_3 \in \mathbb{R}^{3\times 6}$ select the first and last three components of $\boldsymbol{r}$, respectively.

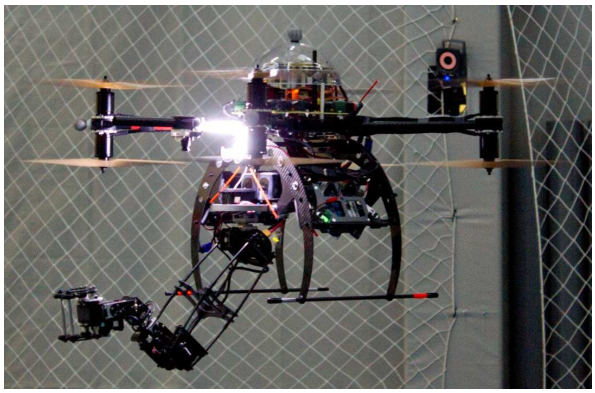

Fig. 3. ARCAS multirotor with the attached 6-DoF manipulator

IV. Experimental Validation

A. Equipment

The ARCAS multirotor is an eight rotor aircraft in coaxial configuration with a tip-to-tip wingspan of 105 cm, 13-inches propellers, height of 50 cm and mass of 8.2 kg including the Lithium Polymer batteries and the robotic arm (see Fig. 3). The autopilot in use, which has been fully developed in CATEC [18] , allows full control of all the hardware and software in order to integrate the robotic arm and the algorithms written in this paper. In order to test all these algorithms, the ARCAS project is using a Model-Based Design (MBD) methodology [19] established on Simulink code generation tools that have proved to be very reliable, fast and convenient. For costly computing code, such as image processing, the vehicle has an i7 Asctec Mastermind on board. In the configuration for this paper, Vicon [20] is used as the positioning system. Vicon is running at 100 Hz and it is only sending the position of the multirotor, as the attitude is obtained with an estimator using the IMU data.

A 6-DoF manipulator [21], whose servos are updated at 50 Hz, is attached to the multirotor. The multi-joint arm is an articulated component that contains all the manipulator DoFs. It includes a first section with two motorized joints (yaw and pitch), followed by an elongated structure. A second section composed of a chain of four motors driving the remaining joints (in sequence pitch, roll, pitch, roll) is present. The manipulator direct kinematic model is obtained by using the well known Denavit-Hartenberg (D-H) method [8]. Coordinate frames associated to each DoF and the corresponding links are represented in Fig. 4.

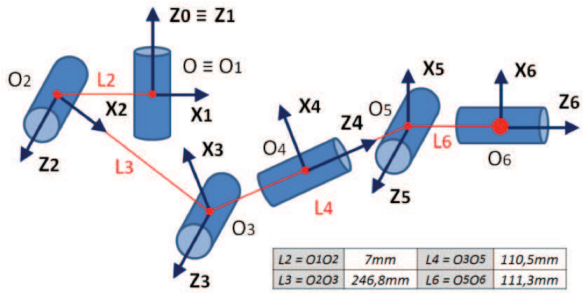

Fig. 4. Coordinates frame for D-H method. The y-axis is not represented for clarity. Frame $\{O, X_0, Y_0, Z_0\}$ is the reference fixed axes system.

Robotis-Dynamixel DC servomotors are selected for driving the manipulator joints. In particular, MX-serie servos (MX-106, MX-64 and MX-28) are used for being small, lightweight and having a geometry that facilitates the installation. They use half duplex asynchronous serial communication and allow configuring an internal PID controller.

B. Control Architecture

A special control architecture has been developed in order to effectively control an aerial platform with a 6-DoF arm. The ARCAS control layer architecture is composed by four main modules (Fig. 5). A specific module is used for the robotic arm, while the remaining modules are traditional in a multirotor controller. However, they have been modified to adapt them to the ARCAS system.

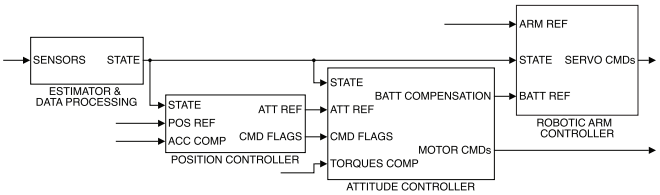

Fig. 5. Main control modules of the ARCAS architecture

1) Estimator & Data Processing Module: This module is in charge of estimating and processing the state of the vehicle (position, linear velocity, attitude, angular velocity, servos data, sensors and safety operator radio references). As inputs it receives all the sensor data on-board the platform.

2) Position Controller Module: The position controller module takes care of the aerial platform stabilization and its outputs are the references for the attitude controller. For this purpose, the controller needs the state of the platform, the position reference given by the high-level controller and compensation terms coming from the multilayer architecture. In the first part, the references given to the platform are smoothed to make a coordinated movement with a controlled acceleration and velocity in the three axes plus the yaw. In addition it performs more complex operations like taking

off and landing. In the second part, it receives the positions errors as inputs for the controller. The compensation signal coming from the third layer is added to the output of basic PIDs (layer 0, see [14] for implementing details) to reject the perturbations coming from the arm movement.

3) Attitude Controller Module: The attitude controller module runs the lowest level controller of the platform. It receives references from the position controller and stabilizes the platform sending a control signal to each of the eight motors. It also runs a special compensator module (see Section III) to take into account the movements of the arm.

The safety and manual module (see Fig. 6) is responsible of the manual control of the platform and the safety management of the aircraft motors. The attitude control receives the state (attitude) of the platform and the reference from its previous block and generates an angular velocity reference signal by means of a PID controller (layer 0). The inputs for the angular velocity control are the current angular velocity and the reference rates. The outputs are the thrust and the torques needed to reach the mentioned references. The functionalities of the robotic arm compensator module (layers 1 and 2) has been instead deeply described in Section III. Estimations from layer 3 are also taken into account as inputs. Finally, the saturations and mixer module parses the commanded thrust and torques to motor signals references.

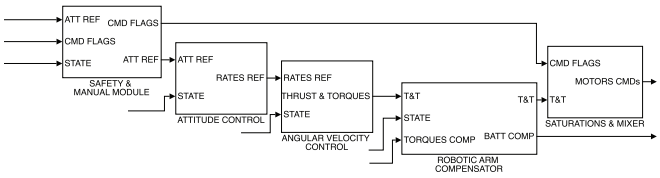

Fig. 6. Attitude controller module

4) Robotic Arm Controller Module: The robotic arm controller module is in charge of the final checks of the references given to the arm, its deployment, retraction and parsing the values to servo control signals. In addition there is an emergency state in which the arm is retracted at a very high velocity. A safety block always checks the references received from the high level controller. This module first checks that there is no angular reference out of mechanical bounds. Therefore, it checks the presence of possible self-collisions and finally verifies that there is no conflict with any part of the platform; otherwise, the arm is stopped until a valid command is received.

C. Case studies

The multilayer control system proposed in Section III has been experimentally tested on the robot described in Section IV-A. The main control goal is to keep fixed the multirotor CoG while the attached manipulator is performing a certain given trajectory. Four case studies are considered. First, each layer introduced in Section III is disabled, i.e., $\boldsymbol{f}_2 = \boldsymbol{f}_3 = \boldsymbol{\tau}_2 = \boldsymbol{\tau}_3 = \mathbf{0}_3$ in (2), and then the multirotor is controlled only through the basic PID control (layer 0). In the second case, the first layer is activated, meaning that the battery compartment moves to counteract the arm behaviour. In the third case, both the battery movement and the arm static compensation layers are active, i.e., only $\boldsymbol{f}_3$ and $\boldsymbol{\tau}_3$ in (2) are forced to be zero. In the latter case, all the layers are active. For all the case studies, the terms β_i, with $i = \{0, 2, 3\}$, in Section III have been chosen to 1 so as to weight in the same manner the contribution of each layer.

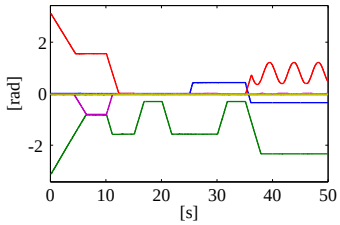

Fig. 7. Commanded joint positions of the attached arm. From the first to the sixth joint, the color legend is: blue, green, red, cyan, magenta, olive.

The movements of the manipulator's joints are planned as in Fig. 7. In detail, the manipulator starts in the retracted position and reaches a certain deploying configuration as soon as the experiment starts. Each 5 seconds the configuration of the arm changes trying to excite its dynamics and then the effects on the aerial platform. After six different configurations, the third joint starts to behave like a pendulum. Finally, the experiment ends. During each movement, the commanded velocity for each joint is 40 degrees per second[3].

In the following, each case study is detailed through the related plots and comments. In the multimedia attachment the performance of the system is also compared.

1) Case Study A: In this case study only the basic PID control (layer 0) for the multirotor is active. Figure 8 illustrates the plots of the performed experiment. The multirotor is commanded to hover in a certain position while the manipulator performs the planned movements. The position error norm of the multirotor CoG with respect to the inertial frame is illustrated in Fig. 8(a): the peaks reach about 30 cm. Figure 8(b) illustrates the roll and pitch multirotor attitude with respect to the inertial frame: in hovering, such angles should be null as much as possible. Figures 8(c) and 8(d) show the given control thrust and torques, respectively.

2) Case Study B: The first control layer is now active: the battery compartments moves to counterbalance the manipulator effects on the aerial platform. The plots summarizing the performed experiments are depicted in Fig. 9. The position error norm of the multirotor CoG is shown in Fig. 9(a). The behaviour is better than the previous case study, but the peaks remain relevant (about 25 cm). The movement of the battery on the slider mechanism is depicted in Fig. 9(b), that is the projection of $\boldsymbol{p}_B^{b^*}$ in (5) along the battery axis. The introduced novelty is very interesting from a mechanic point of view, but alone it is not enough to compensate the variety of the movements that a manipulator might perform. This limitation

[3]This velocity is high with respect to possible on-site aerial manipulation tasks, but it has been chosen is such a way to stress the effects of dynamic forces induced on the aerial platform.

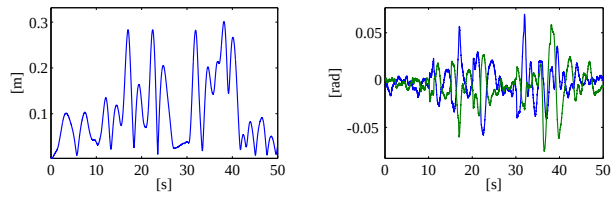

(a) Position error norm. (b) Multirotor attitude.

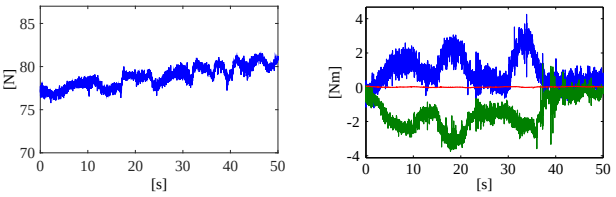

(c) Given thrust. (d) Given torques

Fig. 8. Case study A. Only layer 0 is active. Subfigure (a) shows the position error norm of the multirotor CoG. Subfigure (b) illustrates the roll (blue) and pitch (green) angles. Subfigures (c) and (d) show the given thrust u and torques $\boldsymbol{\tau}_b^b$, respectively. The legend for Subfigure (d) is: roll component of $\boldsymbol{\tau}_b^b$ in blue, the pitch is in green, the yaw in red.

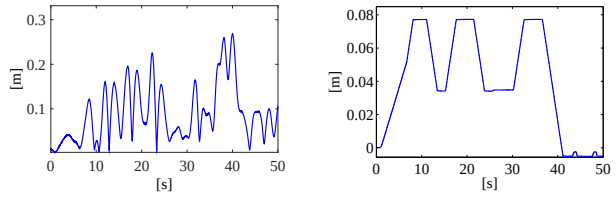

(a) Position error norm. (b) Battery movement.

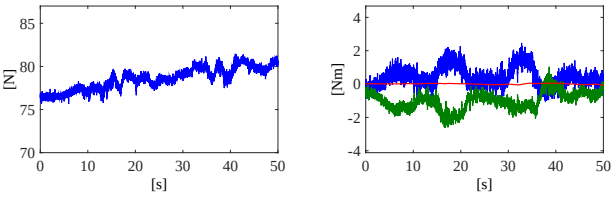

(c) Given thrust. (d) Given torques

Fig. 9. Case study B. The battery movement compartment is now moving. Subfigure (a) shows the position error norm of the multirotor CoG. Subfigure (b) illustrates the battery movement on its slider. Subfigures (c) and (d) show the given thrust and control torques, respectively. The legend for Subfigure (d) is: roll component of $\boldsymbol{\tau}_b^b$ in blue, the pitch is in green, the yaw in red.

of the introduced mechanism justifies the introduction of the other control layers. Given control thrust and torques are depicted in Fig.s 9(c) and 9(d), respectively. Multirotor attitude is similar to Case Study A.

3) Case Study C: The active static compensation layer is now employed together with the battery movement. The plots related to the performed experiment are illustrated in Fig. 10. The position error norm, Fig. 10(a), is now much better than the previous two cases (about 8 cm as maximum), meaning that the effects at least of the manipulator statics has been successfully compensated. The roll and pitch angles peaks in Fig. 10(b) are half with respect to Case Study A: the aerial vehicle has to move less to maintain its CoG close as much as possible to the commanded hovering position. The

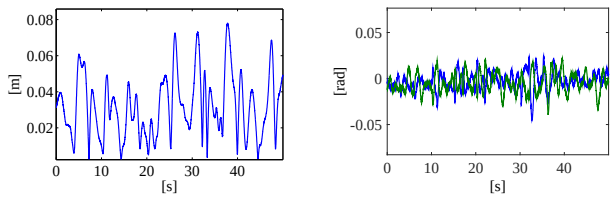

(a) Position error norm. (b) Multirotor attitude.

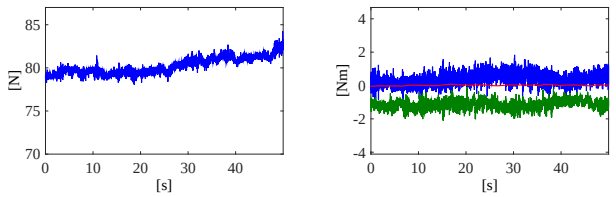

(c) Given thrust. (d) Given torques

Fig. 10. Case study C. Both static compensation and battery compartment movement are active. Subfigure (a) shows the position error norm of the multirotor CoG. Subfigure (b) illustrates the roll (blue) and pitch (green) angles. Subfigures (c) and (d) show the given thrust and control torques, respectively. The legend for Subfigure (d) is: roll component of $\boldsymbol{\tau}_b^b$ in blue, the pitch is in green, the yaw in red.

given thrust, Fig. 10(c), and torques, Fig. 10(d), are more demanding with respect to the previous two case studies, but still affordable for the employed system. Battery movement is comparable to Case Study B.

4) Case Study D: Each layer of the proposed architecture is now finally active. In particular, the estimator of external forces and moments is employed to compensate the effects due to both the inaccurate UAV modeling and the manipulator dynamics. The experimentally tuned gains in (9) have been set to $\boldsymbol{K}_1 = \text{diag}(\begin{bmatrix}14 & 14 & 16 & 24 & 24 & 4.5\end{bmatrix})$ and $\boldsymbol{K}_2 = \text{diag}(\begin{bmatrix}3.5 & 3.5 & 4 & 6 & 6 & 1.39\end{bmatrix})$. A second order Butterworth filter is employed to smooth the estimations that are fed back to the controller.

As visible from Fig. 11(a), the error norm about the hovering position of the aerial vehicle is the lowest among all the considered case studies (about 6 cm as maximum). To maintain as much as possible the multiorotr CoG close to the commanded hovering position, the aerial vehicle has to perform quick movements to counterbalance both the statics and the dynamics of the moving manipulator arm. This is highlighted in the attitude roll and pitch behaviour depicted in Fig. 11(b), and in the total commanded thrust and torques shown in Fig.s 11(c) and 11(d), respectively. Battery movement is comparable to Case Study B. The estimated external forces and moments are represented in Fig.s 11(e) and 11(f), respectively. Two considerations have to be done. First, the estimator initial conditions are null, as underlined in (9). However, the estimating process starts when the aerial vehicle takes off. In the represented plots, instead, the starting time for the task is when the robotic arm starts to be deployed. Second, it is possible to observe a slow drift-like effect in Fig. 11(e) concerning the z component of the estimated external forces. This is mainly due to a recirculation wind flow due to the indoor arena and generated

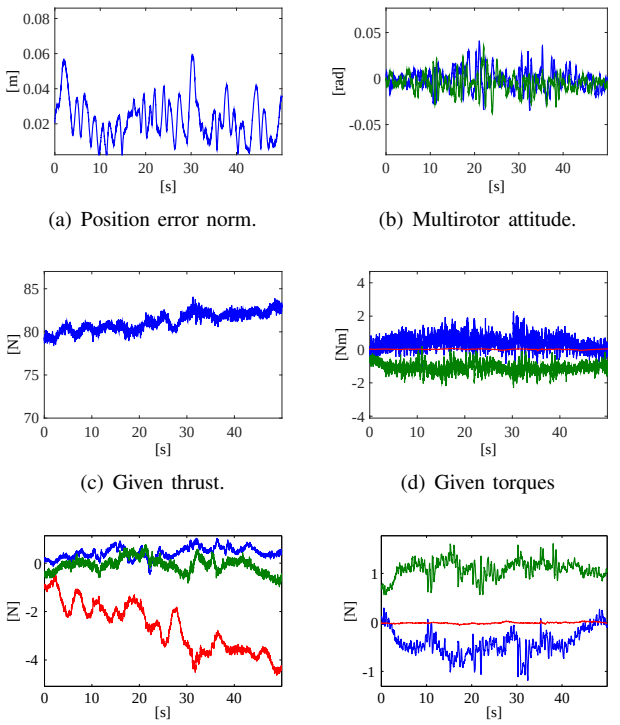

(a) Position error norm. (b) Multirotor attitude.

(c) Given thrust. (d) Given torques

(e) Estimated external forces. (f) Estimated external moments

Fig. 11. Case study D. All the control layers are active. Subfigure (a) shows the position error norm of the multirotor CoG. Subfigure (b) illustrates the roll (blue) and pitch (green) angles. Subfigures (c) and (d) show the given thrust and control torques, respectively. The legend for Subfigure (d) is: roll component of $\boldsymbol{\tau}_b^b$ in blue, the pitch is in green, the yaw in red. Subfigures (e) and (f) illustrate the unfiltered estimated external forces and moments, respectively. Subfigure (e) depicts the estimated force along x (blue), y (green) and z (red) axes of body frame. The legend for Subfigure (f) is: the roll component of the estimated external moments is in blue, the pitch is in green and the yaw in red.

in the time frame of the experiment by the eight propellers.

Finally, considering a comparison between the averages of the position error norms of the multirotor CoG in each of the case studies (Case study A: 10.4 cm; Case Study B: 8.93 cm; Case Study C: 3.2 cm; Case Study D: 2.25 cm), it is evident how adding each layer in the control structures improves the performance of the UAV control. In particular, the big change appears when the full static software compensation is introduced together with the moving battery mechanism. The proposed estimator reduces the remaining dynamic effects.

V. Conclusion and Future Work

A multilayer architecture to control multirotor UAVs equipped with a servo robot arm is proposed in this paper. Although the work has been focused on the architecture employed in the ARCAS project, the topic of the work remains general and it can be applied to any kind of UAV equipped with a servo robot arm. Future work will be focused on considering the battery as another degree of freedom to synchronize its movement with the ones of the manipulator joints, Moreover, the proposed estimator of external generalized forces will be improved taking into account the entire dynamic model of the arm.

References

[1] V. Lippiello and F. Ruggiero, "Exploiting redundancy in Cartesian impedance control of UAVs equipped with a robotic arm," in *2012 IEEE/RSJ International Conference on Intelligent Robots ans Systems*, Vilamoura, P, 2012, pp. 3768–3773.

[2] V. Lippiello and F. Ruggiero, "Cartesian impedance control of a UAV with a robotic arm," in *10th International IFAC Symposium on Robot Control*, Dubrovnik, HR, 2012, pp. 704–709.

[3] T. Madani and A. Benallegue, "Sliding mode observer and backstepping control for a quadrotor unmanned aerial vehicles," in *Proceedings of the 2007 American Control Conference*, New York City, NY, 2007, pp. 5887–5892.

[4] J. Jimenéz-Cano, J. Martin, G. Heredia, A. Ollero, and R. Cano, "Control of an aerial robot with multi-link arm for assembly tasks," in *2013 IEEE International Conference on Robotics and Automation*, Karlsruhe, G, 2013, pp. 4916–4921.

[5] V. Lippiello, G. Loianno, and B. Siciliano, "MAV indoor navigation based on a closed-form solution for absolute scale velocity estimation using optical flow and inertial data," in *50th IEEE Conference on Decision Control and European Control Conference*, Orlando, FL, 2011, pp. 3566–3571.

[6] R. Carloni, V. Lippiello, M. D'Auria, M. Fumagalli, A. Mersha, S. Stramigioli, and B. Siciliano, "Robot vision: Obstacle-avoidance techniques for unmanned aerial vehicles," *IEEE Robotics & Automation Magazine*, vol. 20, no. 4, pp. 22–31, 2013.

[7] R. Mahony, S. Stramigioli, and J. Trumpf, "Vision based control of aerial robotic vehicles using the port Hamiltonian framework," in *50th IEEE Conference on Decision Control and European Control Conference*, Orlando, FL, 2011, pp. 3526–3532.

[8] B. Siciliano, L. Sciavicco, L. Villani, and G. Oriolo, *Robotics: Modelling, Planning and Control*. London, UK: Springer, 2008.

[9] [Online]. Available: http://www.arcas-project.eu

[10] S. Kim, S. Choi, and H. Kim, "Aerial manipulation using a quadrotor with a two DOF robotic arm," in *2013 IEEE/RSJ International Conference on Intelligent Robots and Systems*, Tokyo, J, 2013, pp. 4990–4995.

[11] H. Yang and D. Lee, "Dynamics and control of quadrotor with robotic manipulator," in *2014 IEEE International Conference on Robotics and Automation*, Hong Kong, C, 2014, pp. 5544–5549.

[12] C. Korpela, M. Orsag, and P. Oh, "Towards valve turning using a dual-arm aerial manipulator," in *2014 IEEE/RSJ International Conference on Intelligent Robots and Systems*, Chicago, IL, USA, 2014, pp. 3411–3416.

[13] G. Emray and G. Katherine, "Autonomous payload parsing management system and structure for an unmanned aerial vehicle," U.S. Patent US2 011 084 162, 2011.

[14] F. Ruggiero, J. Cacace, H. Sadeghian, and V. Lippiello, "Impedance control of VTOL UAVs with a momentum-based external generalized forces estimator," in *2014 IEEE International Conference on Robotics and Automation*, Hong Kong, C, 2014, pp. 2093–2099.

[15] B. Yuksel, C. Secchi, H. Bulthoff, and A. Franchi, "A nonlinear force observer for quadrotors and application to physical interactive tasks," in *2014 IEEE/ASME International Conference on Advanced Intelligent Mechatronics*, Besacon, F, 2014, pp. 433–440.

[16] K. Nonami, F. Kendoul, S. Suzuki, and W. Wang, *Autonomous Flying Robots. Unmanned Aerial Vehicles and Micro Aerial Vehicles*. Berlin Heidelberg, D: Springer-Verlag, 2010.

[17] A. De Luca, A. Albu-Schaffer, S. Haddadin, and G. Hirzinger, "Collision detection and safe reaction with the DLR-III lightweight manipulator arm," in *IEEE/RSJ International Conference on Intelligent Robots and Systems*, Beijing, C, 2006, pp. 1623–1630.

[18] "Center for advanced aerospace technologies." [Online]. Available: http://www.catec.aero/en

[19] D. Santamaria, F. Alarcon, A. Jimenz, A. Viguria, M. Béjar, and A. Ollero, "Model-based design, development and validation for UAS critical software," *Journal of Intelligent & Robotic Systems*, vol. 65, no. 1–4, pp. 103–114, 2012.

[20] "Vicon motion systems." [Online]. Available: http://www.vicon.com

[21] R. Cano, C. Pérez, F. Pruano, A. Ollero, and G. Heredia, "Mechanical design of a 6-DOF aerial manipulator for assembling bar structures using UAVs," in *2nd RED-UAS 2013 Workshop on Research, Education and Development of Unmanned Aerial Systems*, Compiegne, F, 2013.